Effects of the Geomagnetic Superstorms of 10–11 May 2024 and 7–11 October 2024 on the Ionosphere and Plasmasphere

Viviane Pierrard *, Tobias G.W. Verhulst, Jean-Marie Chevalier, Nicolas Bergeot, Alexandre Winant

Posted Date: 24 January 2025

doi: 10.20944/preprints202501.1791.v1

Keywords: mother's day; geomagnetic storms; ionosphere; plasmasphere; VTEC

Article

Effects of the Geomagnetic Superstorms of 10–11 May 2024 and 7–11 October 2024 on the Ionosphere and Plasmasphere

Viviane Pierrard [1,2,*], Tobias G.W. Verhulst [3], Jean-Marie Chevalier [4], Nicolas Bergeot [4] and Alexandre Winant [1,2]

[1] Solar Terrestrial Center of Excellence (STCE) and Space Physics, Royal Belgian Institute for Space Aeronomy, Brussels, Belgium
[2] Earth and Life Institute–Climate Sciences ELI-C, Université Catholique de Louvain, Louvain-la-Neuve, Belgium
[3] Solar Terrestrial Center of Excellence (STCE), Royal Meteorological Institute of Belgium, Brussels, Belgium
[4] Solar Terrestrial Center of Excellence (STCE), Royal Observatory of Belgium, Brussels, Belgium
* Correspondence: viviane.pierrard@aeronomie.be

Abstract: On 10 May 2024 at 17h:07 UTC, the arrival of solar a coronal mass ejection (CME) generated the strongest geomagnetic storm of the last twenty years with a minimum Dst = -412 nT, usually referred to as the Mother's Day event. On 10 October 2024, the second strongest event of the solar cycle 25 appeared with Dst=-335 nT, preceded on 8 October by an event with Dst=-153nT. In the present work, we show with measurements of vertical total electron contents and with ionosonde observations from Europe, USA and South Korea that the ionization of the upper atmosphere shortly increased at the arrival of the CME for these different events, followed by a fast decrease at all latitudes. The ionization remained very low for more than a full day. While the recovery appears at the beginning of the second day after the onset for both events in October, the sudden recovery in the middle of the second day on 12 May is much more unusual. The analysis of the observations at different latitudes and longitudes shows that the causes of the ionization variations during the superstorms were mainly due strong perturbations in the ionospheric F layer, and amplified by the plasmasphere's influence on the vertical total electron content (VTEC). The erosion of the plasmasphere during these two strong events led to a plasmapause located to exceptionally low radial distances smaller than 2 Re (Earth's radii) in the post-midnight sector, and a rotating plume in the afternoon-dusk sector clearly visible in the BSPM plasmasphere model. Several days after the storms were necessary to recover normal ionization rates.

Keywords: mother's day; geomagnetic storms; ionosphere; plasmasphere; VTEC

1. Introduction: Strongest Storms of Solar Cycle 25

In the present work, we compare the two strongest geomagnetic events of the solar cycle 25 in 2024: the Mother's Day storm on 10-11 May 2024 and the successive storms on 8-11 October 2024. For these events, we compare the observations of solar wind parameters that generate the geomagnetic activity, ionosonde measurements (up to the maximum of electron density in the F layer of the ionosphere), Vertical Total Electron Content (VTEC) up to GNSS (Global Navigation Satellite System) orbit altitude, plasmapause measurements by SWARM satellites, and the BSPM plasmasphere model in order to determine the evolution in time and space of the plasma density variations. The observation methods are described in Section 2, results in Section 3 for 10-11 May 2024 Mother's Day event and Section 4 for 8-11 October 2024 storms, while Section 5 discusses and summarizes the results.

 doi:10.20944/preprints202501.1791.v1

2. Observation Methods

For both periods of geomagnetic disturbances, we describe in this section the models and the methods used to analyse the observations from different instruments that are used in this work.

2.1. Solar Wind and Geomagnetic Indices

OMNI is a multi-source data portal of near-Earth solar wind's magnetic field and plasma parameters provided by NASA. We use it to obtain the solar wind parameters measured at 1 Astronomy Unit (UA) (i.e. the average distance between the Sun and Earth) and the geomagnetic activity indices.

2.2. Vertical Total Electron Content VTEC

One of the parameters used to characterize the ionospheric conditions is the vertical total electron content (VTEC). TEC is the total number of free electrons integrated along the raypath between the GNSS (Global Navigation Satellite System) satellites (located at an altitude between 19,100 km until approximately 23,300 km, thus a radial distance from the center of the Earth of approximately 4 Re) and the receiver on the ground. It is estimated in a unit called TECu in which 1 TECu = 10^{16} electrons/m^2. The VTEC is the vertical value of TEC projected from this raypath intersecting above the electron density peak at 450 km height. The VTEC is directly related to the GNSS signal propagation delay due to the ionosphere. These ionospheric conditions are closely monitored by the STCE in Brussels based on the GNSS observations of the EUREF Permanent Network (Bruyninx, 2019) and using the ROB-IONO software (Bergeot, 2014). With these 30-s GPS+Galileo+GLONASS real-time observations, VTEC maps are estimated every 5 min above Europe. The VTEC variability, reflecting the ionospheric state variations during the 5-min time span of the interpolation, is estimated. The VTEC time series provided in this paper are extracted from these maps at three locations in Figures 4 and 11:

a) in the northern part of Europe (61°N, 5°E),
b) above Brussels, in mid-latitude Europe (50.5°N, 4.5°E),
c) in North Africa (36°N, 5°E).

2.3. Ionosonde Observations

Ionosondes employ high frequency (HF) radio transmissions of various frequencies to determine the electron density profile above the instrument. Frequencies below the plasma frequency $\omega = \sqrt{\frac{N_e e^2}{\varepsilon_0 m}}$ (where e is the electron charge, m its mass, ε_0 is the permittivity of free space) are reflected by the plasma in the ionosphere. Therefore, the electron density profile $N_e(h)$ can be reconstructed from the reflection of a range of different frequencies. The main limitation of this technique is that it allows observations only up to the height of the greatest electron density. This altitude varies significantly both during quiet conditions, and as a result of particular disturbances such as geomagnetic storms.

In the present study, we use data from three ionosondes in Europe (JR055, DB049, EB040), at different latitudes, as well as two ionosondes in other longitude sectors: IC437 in South Korea and MHJ45 in the USA. Ionograms were obtained from the DIDBase of the GIRO repository (Reinisch and Galkin, 2011). This allows us to compare the storm effects at different latitudes as well as the effect of the local time at the onset of the event. The coordinates of the observatories are listed in Table 1. Each of these observatories uses a similar Digisonde DPS-4D ionosonde, and produces regular soundings of the ionosphere at intervals of 5 (for the European observatories) or 7.5 min (for the American and South Korean observatories). All ionograms were manually inspected in order to derive the characteristics of the various layers (we use here the critical frequencies foF_1 and foF_2 of the two F-region density peaks), with only data points retained which could be obtained reliably according to the standard URSI (International Union of Radio Science) rules.

 doi:10.20944/preprints202501.1791.v1

Table 1. Ionosondes from which data is used.

Name	URSI code	Latitude	Longitude
Juliusruh	JR055	54.60°N	13.40°E
Dourbes	DB049	50.10°N	4.60°E
Roquetes	EB040	40.80°N	0.50°E
Millstone Hill	MHJ45	42.60°N	288.50°E
I-Cheon	IC437	37.14°N	127.54°E

The exceptional ionospheric conditions during the events analysed here cause some particular difficulties in the interpretation of the ionograms. There are three reasons for occasional gaps in the time-series of the critical frequencies. First, during the night-time, spreading of the F_2 trace is observed (see the left panel of Fig. 1 for an example). This can render it impossible to determine accurately the critical frequency foF_2. During the first night of the 11 May storm, there were also sporadic E layers observed produced by particle impacts (which are associated with the visible auroras seen at those same times even at low latitudes). An example of this is shown in Fig. 1 on the right. In this example, the Es layer extends to above 4 MHz, making it impossible to detect the depleted F layer above.

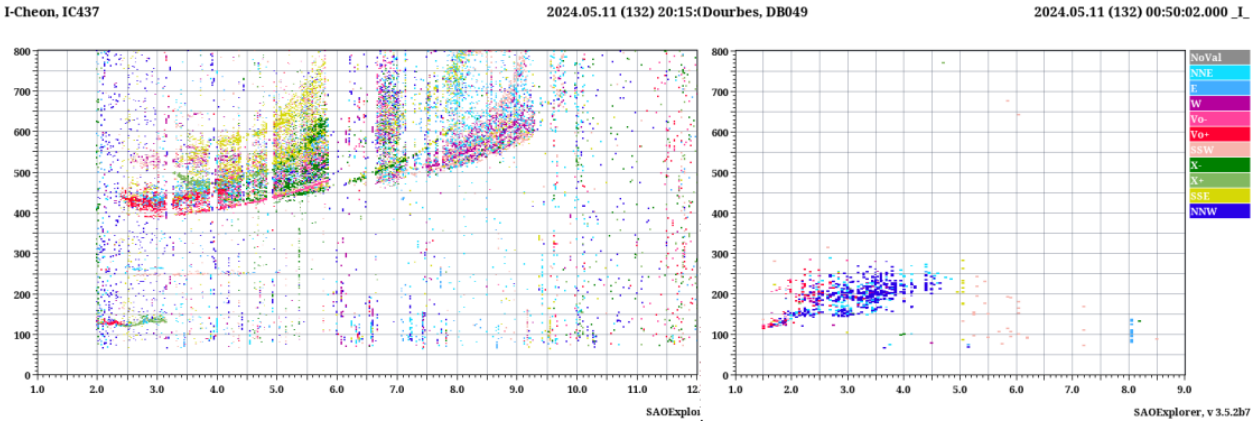

Figure 1. Examples of spread-F condition (left, recorded by IC437 on 11 May 2024 at 20:15:00 UTC) and particle-induced Es-layer (right, recorded by DB049 on 11 May at 00:50:02 UTC). Note that the height (vertical axis) ranges from 0 to 800 km in both cases, but the frequencies (horizontal axis) from 1 to 12 MHz in the left panel and from 1 to 9 MHz in the right panel.

Finally, there are some gaps in the data related to absorption of the ionosonde signals in the D region of the ionosphere during flares. On 11 May 2024, there was an X5.89 flare peaking at 01:23 UTC (Universal Time Coordinated) and an X1.54 flare peaking at 11:44 UTC. In addition, during the period of interest, there were some M-class flares as well. For most of 11 May, even the minima of the X-ray flux remained above the level of an M1 flare. Depending on the signal-to-noise ratio usually obtained by the different ionosondes, and the local time at each during the flares, this absorption in the lower ionosphere results in gaps in the observation of the F layer.

2.4. Plasmasphere Model and Data

The Belgian SWIFF Plasmasphere Model (BSPM) is a 3D-Kinetic semi-empirical model of the plasmasphere (Pierrard and Stegen, 2008), coupled to the ionosphere (Pierrard and Voiculescu, 2011). It has recently been improved to take into account the most recently identified relevant physical processes (Pierrard et al., 2021a). It can be run for any date to obtain every hour the number density and temperature of the electrons and protons inside and outside the plasmasphere, as well as the position of the plasmapause, as a function of the geomagnetic activity driven by the Kp index. It uses the kinetic approach for the particle densities and the mechanism of quasi-interchange instability for the formation of the plasmapause. The density in the plasma trough region has recently been improved using observations of Van Allen Probes (Botek et al., 2021). The results of the plasmasphere

 doi:10.20944/preprints202501.1791.v1

model have been compared to NASA's IMAGE mission (2000-2005) global EUV images of the plasmasphere (Pierrard and Cabrera, 2005), Cluster (Verbanac et al. 2015) and Themis (Bandic et al., 2017), among others, allowing to validate the plasmasphere erosion and dynamical evolution.

Moreover, the magnetic and plasma observations of the low-Earth orbiting SWARM satellites allow us to derive the midnight plasmapause (Heilig et al., 2022). Launched on 22 November 2013 into a near-polar Low Earth Orbit (LEO), SWARM is a constellation of three identical satellites operated by the European Space Agency (ESA) with the purpose of mapping Earth's magnetic field (Olsen et al., 2013). The initial altitude of the satellite pair SWARM A and SWARM C was about 490 km in April 2014 and it was about 510 km for SWARM B, both orbit altitudes do slowly decay with time. Based on in situ electron density and temperature (Knudsen et al., 2017), GPS-derived TEC, and auroral field-aligned current observations at the SWARM satellites, new SWARM products have recently been developed to characterize plasmapause-related boundaries in the topside ionosphere. This product also includes a plasmapause index, a proxy for the midnight plasmapause position. This index is derived from SWARM observations similarly as described in Heilig and Lühr (2018).

3. Mother's Day Storm: 10-11 May 2024

3.1. Observed Solar Wind and Geomagnetic Indices

An exceptionally strong geomagnetic storm occurred during the night from 10 to 11 May 2024, with auroras observed everywhere in Europe (Karan et al., 2024). It has been called the Mother's Day event due to the date corresponding to Mother's Day in many countries in the world. This was the strongest storm for the last twenty years with a minimum of Disturbed Storm Time index Dst < -400 nT. Due to the varying speeds and quick succession of different Coronal Mass Ejections (CMEs) coming from the active region NOAA 13664, several of them merged and interacted as they travelled through the interplanetary medium, leading to enhanced effects in the Earth's space environment (Pierrard et al., 2024). These CMEs were associated to X2.2 flare on 9 May and three X1 flares on 8 May.

The characteristics of the solar wind when it reached 1 AU, obtained from OMNI, are shown in Figure 2. The bulk velocity of the solar particles reached more than 1000 km/s (see Figure 2, 2nd panel), and peaks of high temperature > 10^6 K were observed (panel 4). The high-density peak (panel 1) at the arrival of the hot plasma shows the apparition of a shock. The pressure (panel 3) combines the density and velocity effects, and determines the position of the magnetopause. The downward peak of the Z component of the Interplanetary Magnetic Field Bz (panel 5) shows a southward direction that can explain the strong answer of the terrestrial magnetic field (Pierrard, 2024).

The arrival time of enhanced solar plasma at 1 AU with regard to density, velocity and pressure is 10 May 2024 at 17:07 UT. It directly caused the sudden commencement of the strong geomagnetic storm (see Figure 3), followed by the main phase when the Dst index decreased down to a minimum value of -412 nT (see panel 3) in the night of 11 May and the planetary geomagnetic activity index of Kp increased to the maximum value of 9 (panel 1). The geomagnetic activity indices Kp, Ap in nanoTesla (that reached 400 nT, see panel 2), and Dst (also in nT) are illustrated in Figure 3, together with the F10.7 solar *radio flux* at 10.7 cm (panel 4) and intensity of Lyman alpha line in the solar spectrum (panel 5) that are daily solar activity indices.

 doi:10.20944/preprints202501.1791.v1

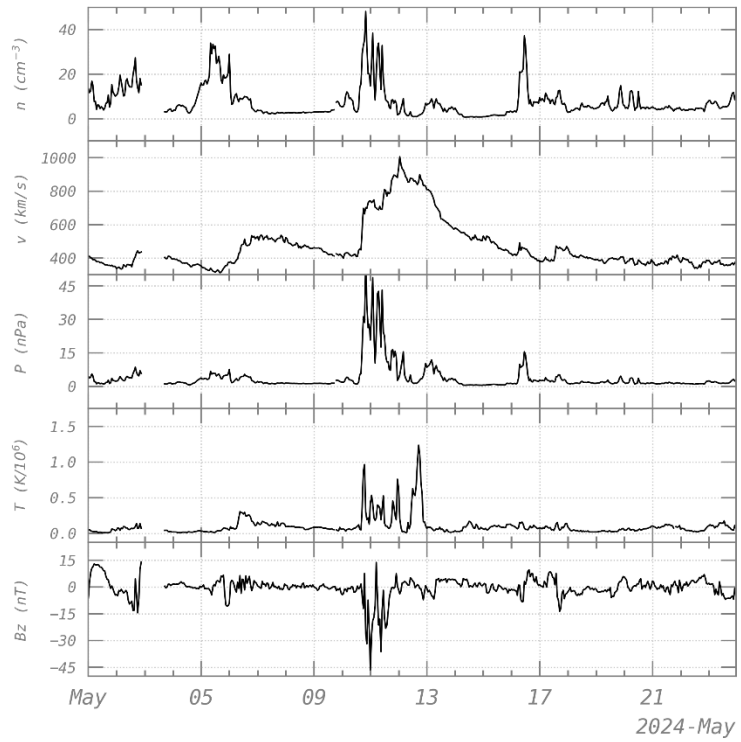

Figure 2. Solar wind density n (top), bulk velocity v (2nd panel), pressure P (3rd panel), proton temperature T (4th panel) and Southward component of the Interplanetary Magnetic Field Bz (bottom panel) from 1 to 24 May 2024 observed by OMNI at 1 AU.

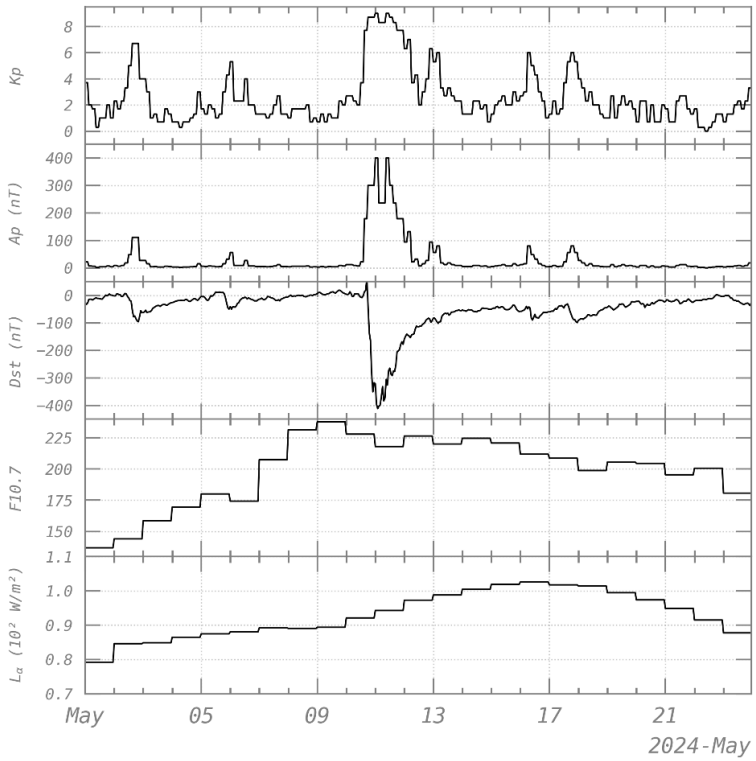

Figure 3. Geomagnetic activity indices of Bartels Kp (top panel), Ap in nT (2nd panel), Disturbed Storm time Dst in nT (3rd panel), daily solar activity indices F10.7 solar *radio flux* at 10.7 cm (4th panel), and intensity of Lyman alpha line in the solar spectrum (bottom panel) from 1 to 24 May 2024.

 doi:10.20944/preprints202501.1791.v1

3.2. Ionospheric Vertical Total Electron Content

Figure 4 shows the time series of the VTEC (in red), the expected VTEC based on observations during the previous 15 days (in grey, with standard variation), and the 5-min VTEC variability (in blue) in the North of Europe, Middle of Europe (Brussels) and more Southward (North of Africa). The three near-real time VTEC time-series showed abnormal variations during the night of 10 to 11 May 2024 followed by a long depletion in VTEC until the 12 May 2024. This is due to the strong CME impact detected during the afternoon of 10 May. By comparing with Figure 3, these VTEC fluctuations (high variations during the storm and long depletion after) can not be explained by variations in F10.7 during these days.

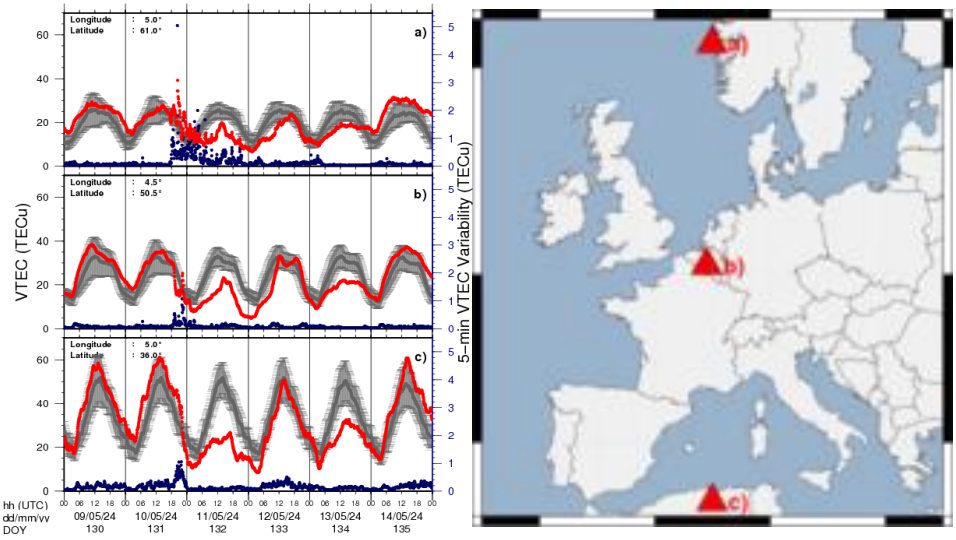

Figure 4. VTEC time series at 3 locations in Europe from 9 to 14 May 2024. The left panel shows the time evolution of the Vertical Total Electron Content (VTEC) (in red) at three locations illustrated in the right panel on a map of Europe: a) in the northern part of Europe (61°N, 5°E), b) above Brussels (50.5°N, 4.5°E), c) in North Africa (36°N, 5°E).

Consequently, the geomagnetic storm had a strong impact on the ionospheric electron content, with sudden increases and decreases of 20 TECu from 18:00 UTC 10th May to 12:00 UTC 11th May in the North of Europe. At mid-latitude, the VTEC tends to decrease starting at 18:50 UTC with a minimum of -10 TECu w.r.t. expected quiet ionosphere and with a sudden peak of increase of 8 TECu (w.r.t. quiet ionosphere) at 22:20 UTC. At the same time, at low latitude, VTEC starts to decrease w.r.t. quiet ionosphere. For both mid- and low latitudes, the VTEC variability also remains high, until midnight on 11th May. These VTEC variations and rapid variability at these 3 latitudes are due to the injection of the particles associated to the storm and leading to the occurrence of auroras at unusually low latitudes.

The maximum variability in the VTEC is observed at 20:20 UTC (see Figure 5).

Preprints.org (www.preprints.org) | NOT PEER-REVIEWED | Posted: 24 January 2025 doi:10.20944/preprints202501.1791.v1

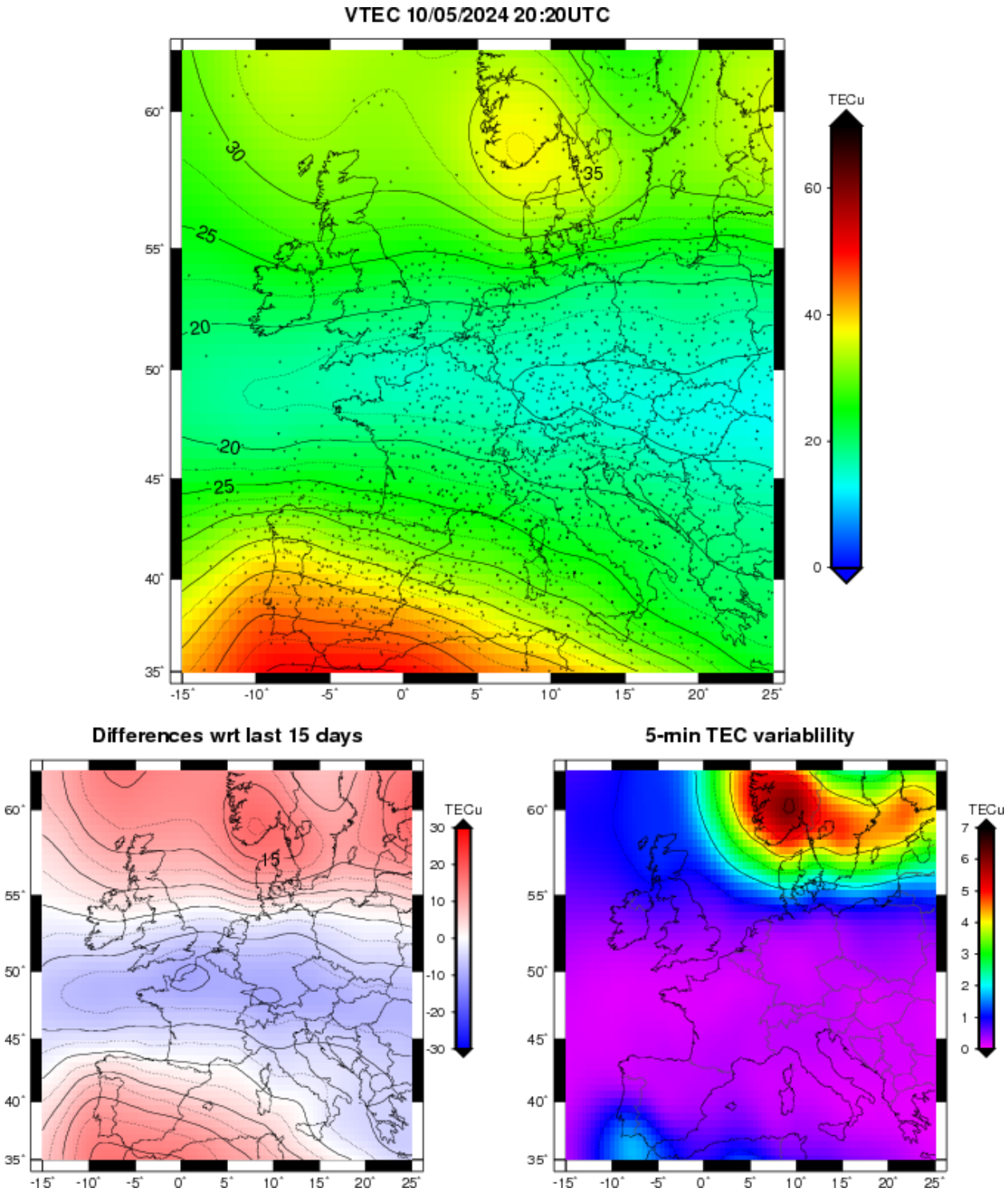

Figure 5. VTEC maps, differences with expected behaviour and variability over Europe on 11th May 2024 at 20:20 UTC. Top: VTEC maps estimated in real-time. The dots represent the VTEC data used for the interpolation. Bottom left: differences between VTEC maps and the expected VTEC (median over the past 15 days). Bottom right: the VTEC variability reflecting the ionospheric state variations during the 5-min time span of the interpolation.

In Figure 5, it can be observed that increase of TEC w.r.t to the quiet ionosphere occurs at high and low latitudes while this is negative at mid-latitude. Over Scandinavia, the VTEC variability reached a maximum 5 TECu for a 5-min interval at 20:20 UTC. This could be linked with the hight values of Rate Of TEC change Index (ROTI) observed in Spogli et al. (2024) supporting the fluctuations implying disturbances in GNSS applications.

 doi:10.20944/preprints202501.1791.v1

The other effect of the storm is the depletion of the VTEC down to 30 TECu at low latitudes until the 12th May around 05:00 UTC. As mentioned in Mendillo (2006) and Bergeot et al. (2013), the persisting depletion in TEC a few days after the onset is due to the contraction of the plasmasphere implying disturbances in the thermosphere circulation and a chemical loss in the ionosphere. This contraction of the plasmasphere is coherent with the observation in Figure 9 Section 3.4 of the present paper.

3.3. Ionosonde Observations

Figure 6 shows the peak electron densities for the F_1 (in blue) and F_2 (in red) layers for the three European ionosondes for a three-day period covering 10 to 12 May 2024. The E-layer (not shown) was found to be not affected by the geomagnetic storm. This is to be expected, because the E-layer is known to be driven entirely by solar irradiance.

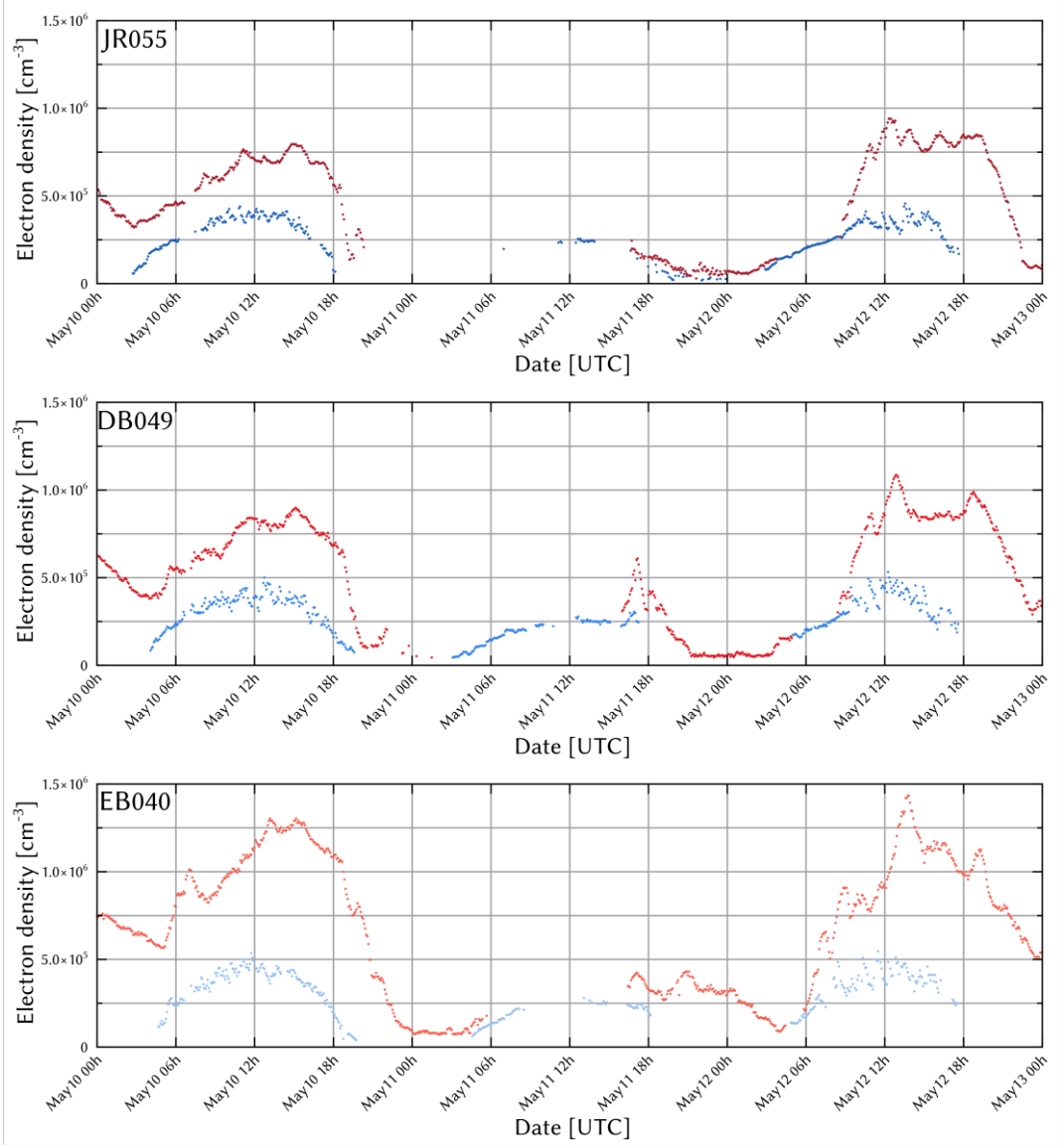

Figure 6. Peak electron densities for F_2 (red) and F_1 (blue) obtained from the ionosonde measurements at Juliusruh (top, JR055), Dourbes (middle, DB049), and Ebre (bottom, EB040) from 10 May 2024 0:00 to 13 May 2024 0:00 UTC.

At the onset of the storm, a very rapid depletion of the F_2-layer density can be observed. The depletion appears to be more rapid at the higher latitudes, although of course the peak density before

 doi:10.20944/preprints202501.1791.v1

the storm is lower at higher latitudes as well. For the most part of 11 May, the F_2 layer was not detected, because the electron density in the F_2 region was lower than in the F_1 layer and thus not visible to the ionosondes. This is referred to as "G-condition" in the ionosonde community, and is often seen during major storms (see for instance Mošna et al. (2024) for some recent examples). The density of the F_1 layer is also seen to be lower than during the quiet day before the storm, but the depletion is much less severe than in the F_2 layer because transport processes and chemical changes are less important at the F_1 layer altitude compared to the influence of solar irradiance.

The strong depletion of the F-region lasts throughout 11 May and morning of 12 May. The reappearance of the F_2 layer on 12 May and its return to quiet time peak density is almost as rapid as the depletion at the onset of the event. This indicates that the refilling of the F_2 layer was very quick. It is also evident that this refilling occurred earlier at the EB040 observatory, which is at the lower latitude. Here, the F_2 layer was detected again around 06 UTC. At the DB049 and JR055 ionosondes at higher latitudes, the F_2 layer was not detected until around 09 UTC, and the peak density reached its climatological values only around noon.

Although the reappearance of the F_2 layer happens earlier at lower latitudes, it can be seen that the peaks of highest electron density reached on 12 May occur earlier at the highest latitude. The highest density is seen on 12 May at 12:20 UTC by JR055, at 12:50 UTC by DB049, and at 13:45 UTC by EB040. This seems to indicate large scale travelling ionospheric disturbances (LSTIDs) moving from the auroral region to lower latitudes. Such LSTIDs are usually seen during the beginning of a storm (e.g. Tsagouri et al., 2023) but seem to occur here also at the time of refilling of the F_2 layer.

Figure 7 shows the critical frequencies of the F_1 and F_2 layers for the Millstone Hill (MHJ45) and I-Cheon (IC437) ionosondes. The behaviour of foF_2 at MHJ45 (top panel) can be seen to be very similar to what was observed by the European ionosondes (see Fig. 6). There is a sudden depletion starting at 18:00 UTC on 10 May, and lasting until 12 May. G-condition was observed for the entirety of 11 May. Around 09:00 UTC on 12 May, there is a sudden increase again of the F_2-layer density. At MHJ45, this corresponds to the normal morning time density increase (as is evident by comparing to the same time on 10 May, which is still before the onset of the storm). This sudden refilling thus occurs at the same time in the European and American sectors, despite the local time difference. The pattern of the F_1 layer at MHJ45 is of course delayed in time compared to the European observatories as a result of this local time difference.

The observations at IC437 (bottom panel of Fig. 7) show a different pattern. A sudden depletion at the storm onset is again evident, but at this location, 18:00 UTC corresponds to nighttime. During the local daytime on the two succeeding days, there are multiple gaps in the data due to the various difficulties explained above. Nevertheless, from those ionograms that could reliably be scaled, it is clear that severe depletion persisted throughout these days, and even during the local night-time on 12 May —the end of the time-series shown in the Figure—, the electron density has clearly not recovered yet to the quiet time level seen before the storm onset. The peaks in foF_2 seen during the local nighttime on 11 May correspond to periods of strong spread-F associated with auroral oval structures expanding to the latitude of this observatory.

 doi:10.20944/preprints202501.1791.v1

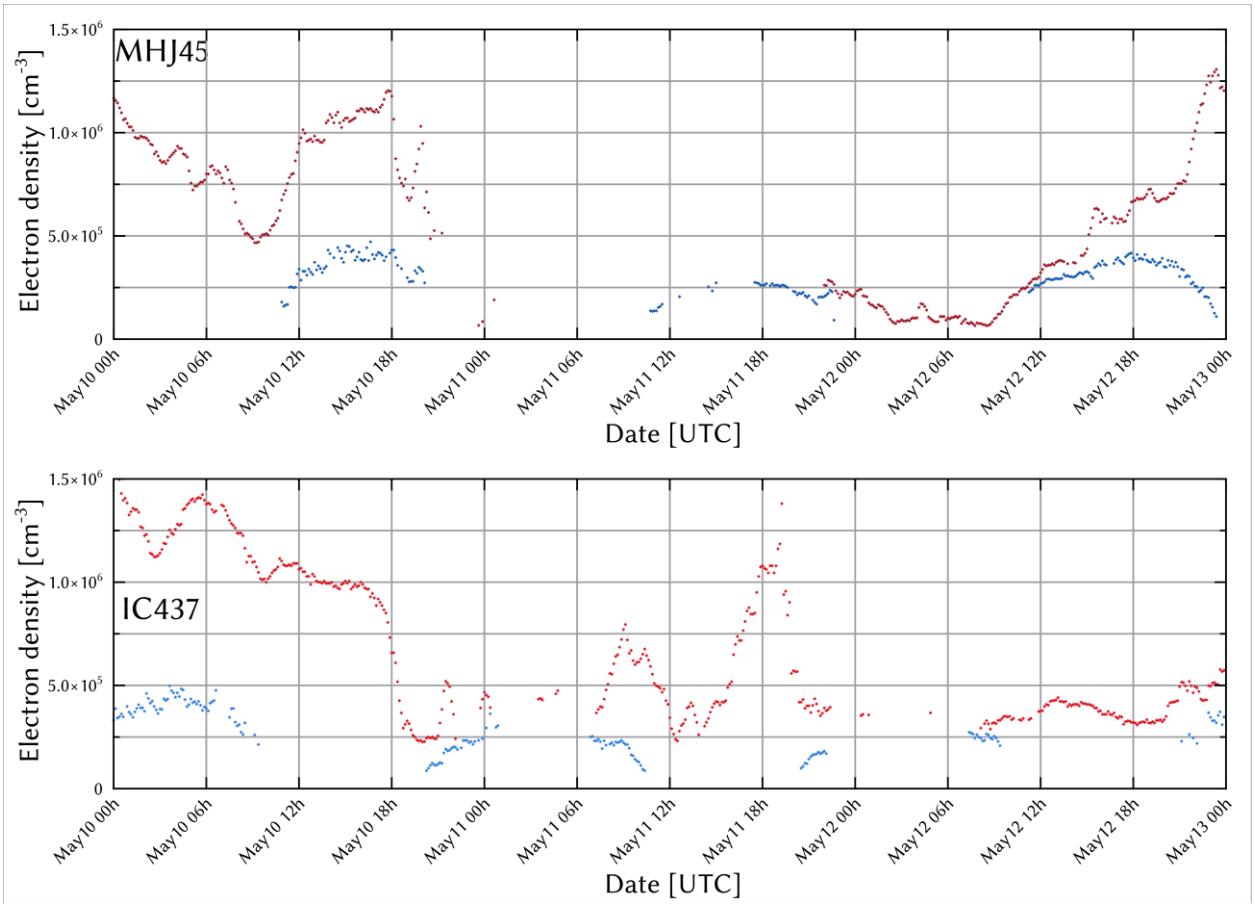

Figure 7. Peak electron densities for the F_2 (red) and F_1 (blue) obtained from the ionosonde measurements at Millstone Hill (top, MHJ45) and I-Cheon (bottom, IC437) from 10 May 2024 0:00 to 13 May 2024 0:00 UTC.

During the main phase of the storm, the electron density and the height of the F region decreased and increased, respectively, indicating an upward displacement of the ionosphere (depression and uplift), irregularities (plasma bubbles) due to stable aurora red arc convergence of low and high latitude effects.

The electron density in the F_2 layer decreased due to the expansion of the atmosphere that modified the recombination time of the ionized particles. During the strong post-storm depletion, F_2 disappeared behind the F_1 layer. The strong spread-F initiated during the main phase was still present during the next nights and caused scintillation of satellite signals. After the arrival of the CME, the electron density decreased and remained significantly lower than during the quiet days, for more than a full day, thus including during the recovery phase of the geomagnetic storm. This meant that for High Frequency (HF) communication, the portion of higher HF frequencies was not available for communication, and so several advisories were sent to civil aviation via PECASUS (https://pecasus.eu/) to warn for this so-called post-storm depression (Kauristie et al., 2021).

Spogli et al. (2024) also showed unusual high spatially distributed values of the Rate Of TEC change Index (ROTI) on the nights of 10 and 11 May. The ROTI enhancements on 10 May might be linked to stable auroral red arcs and an equatorward displacement of the main ionospheric trough. Instead, the ROTI enhancements on 11 May might be triggered by a joint action of low-latitude plasma pushed poleward by the pre-reversal enhancement in the post-sunset hours and wave-like perturbations propagating from the North.

3.4. Plasmasphere

While ionosonde measurements are not affected by the density of electrons in the plasmasphere, this is not the case of VTEC. The sudden but short increase of density observed at the onset of the

 doi:10.20944/preprints202501.1791.v1

storm, in VTEC but not by the ionosondes, indicates that this additional ionization appears above the F2-peak. The plasmaspheric density is thus very important to determine. The sharp density decrease measured by both techniques shows that it takes already place at low altitudes in the F layer. Considering also the plasmasphere erosion appearing during storms (e.g. Pierrard and Cabrera, 2006), VTEC observations allow us to determine the plasmaspheric part in comparison to the ionospheric reduction.

The plasmasphere is the extension of the ionosphere at higher altitude at low and middle latitude (Darrouzet et al., 2009), and its erosion can also explain the reduction of VTEC during and after the storm. Indeed, the extension of the plasmasphere is strongly reduced after storms, with a sharp plasmapause appearing at lower radial distances, as it is illustrated in Figure 8 using the BSPM plasmasphere–ionosphere model (Pierrard et al., 2021a). The top panel shows the extended plasmasphere (orange region with high electron density) before the storm, with an average plasmapause position above 4 Re at all Magnetic Local Time (MLT). The plasmasphere is seen in the geomagnetic equatorial plane (left panel) and in the meridian plane (right panel), with the Sun (thus noon 12:00 MLT) on the left.

The bottom panels show the eroded plasmasphere after the storm, which is very strong due to the Kp reaching the maximum value of 9. The new plasmapause is located around 3 Re in average, but is as low as 2.3 Re in the post-midnight sector, and as high as 5 Re at the endpoint of the plume in the afternoon MLT sector. The plume co-rotates with the Earth after its formation. It takes typically 2 or 3 days after the storm to progressively refill the outer shells of the plasmasphere (Pierrard et al., 2021a).

The plasmasphere erosion after the storm can thus at least partially contribute to the observed VTEC. When the plasmaspause comes closer to the Earth in the equatorial plane (see Figure 8 left bottom panel), the ionospheric trough appears also at lower latitudes (see right bottom panel), due to the motion of the particles along the magnetic field lines (Pierrard and Voiculescu, 2011).

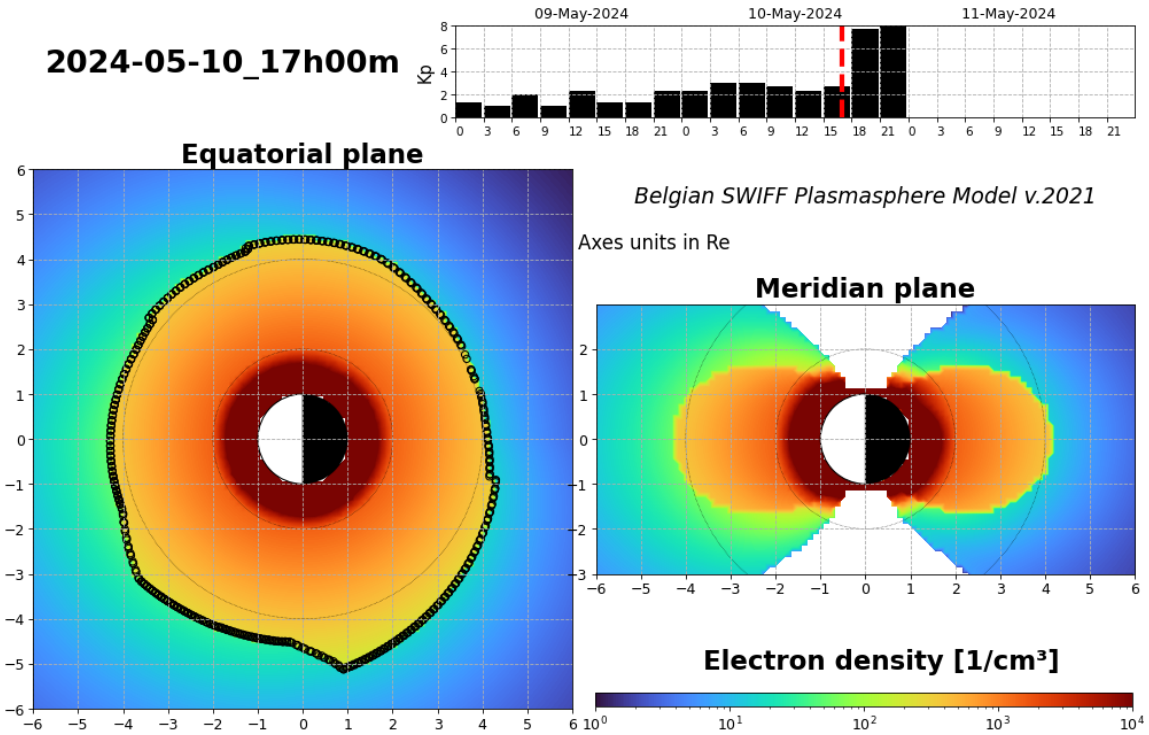

 doi:10.20944/preprints202501.1791.v1

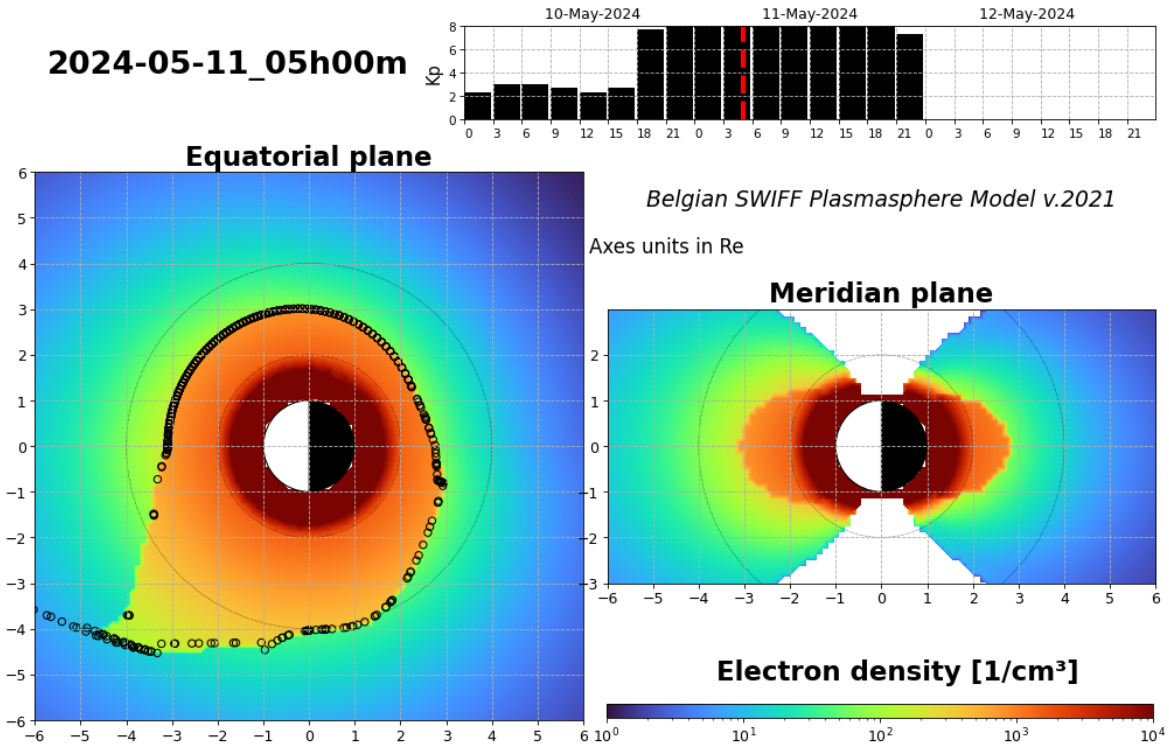

Figure 8. Electron density obtained with the BSPM plasmasphere model coupled to the ionosphere (Pierrard et al., 2021a) on 10 May 2024 at 17:00 UTC (before the storm, top panels) and 11 May 2024 at 5:00 UTC (after the storm, bottom panels). For the two cases, the plasmasphere (orange region) is illustrated in the equatorial plane (left) and in the meridian plane (right). The Bartels geomagnetic index Kp from 1 day before to 1 day after the simulated day is shown in the top panels, with a red dashed line to indicate the exact illustrated time. (esc.pithia.eu).

The midnight plasmapause proxy derived from the magnetic and plasma observation of the low-Earth orbiting SWARM satellites also confirms a very low plasmapause after 11 May 2024 reaching less than 2 Re, as illustrated in Figure 9 (top panel) with the Kp index (bottom panel). Such plasmapauses lower than 2 Re are very rare. The green line corresponds to the midnight plasmapause position and the black lines give the position +/- the standard variation. The squares correspond to the SWARM plasmapause observations. The plasmapause is directly related to the mid-latitude ionospheric trough observed by SWARM (Heilig et al., 2022).

 doi:10.20944/preprints202501.1791.v1

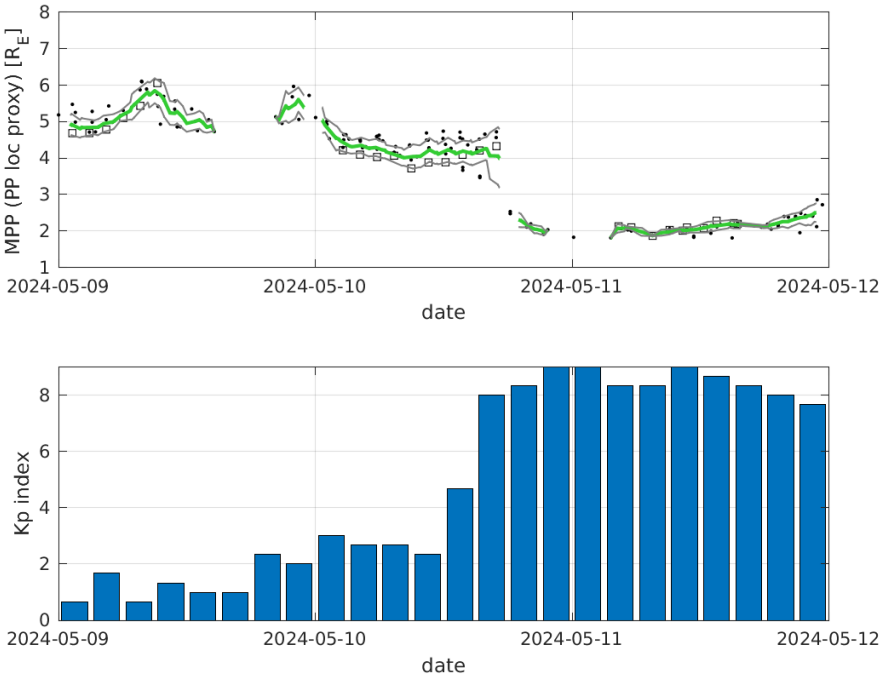

Figure 9. Top panel: Midnight plasmapause proxy derived from the magnetic and plasma observations of the low-Earth orbiting SWARM satellites from 9 to 12 May 2024. Bottom panel: Observed Bartels geomagnetic activity Kp index. (https://swe.ssa.esa.int/elte-plasma-federated).

The position of the plasmapause is crucial because different waves are generated inside and outside the plasmasphere and they affect the particles trapped in the radiation belts (Ripoll et al., 2023; 2024). Several unusual electron belts were observed after the 11 May 2024 geomagnetic storm, as well as a strong increase of the protons from 9.5 to 13 MeV trapped in the South part of the South Atlantic Anomaly (Pierrard et al., 2024).

4. Comparison with Event of 10 to 11 October 2024

4.1. Solar Wind and Geomagnetic Activity Indices

The second most important storm (so far) of the present solar cycle 25 started on 10 October 2024 and reached a minimum of Dst=-335 nT on 11 October 2024. It was preceded by another storm with a minimum Dst=-153 nT on 8 October, as illustrated in Figure 10 (bottom panel) together with the Kp index (5th panel) and the solar wind characteristics that generated these storms: density (1st panel), bulk speed (2nd panel), and temperature (3rd panel). The 8 October storm, associated with a X9 flare on 3 October, is mainly due to the arrival of a high density but low energy particles, while the 11 October storm (associated to a X1.8 flare on 9 October and a X2.1 flare on 7 October) is due to a density peak of energetic particles, as can be seen in the temperature and bulk speed observations. The velocity of the solar wind particles exceeded 700 km/s for this last event. The negative Bz of the interplanetary magnetic field (see 4th panel) explains the high geomagnetic perturbations induced on the terrestrial magnetosphere.

 doi:10.20944/preprints202501.1791.v1

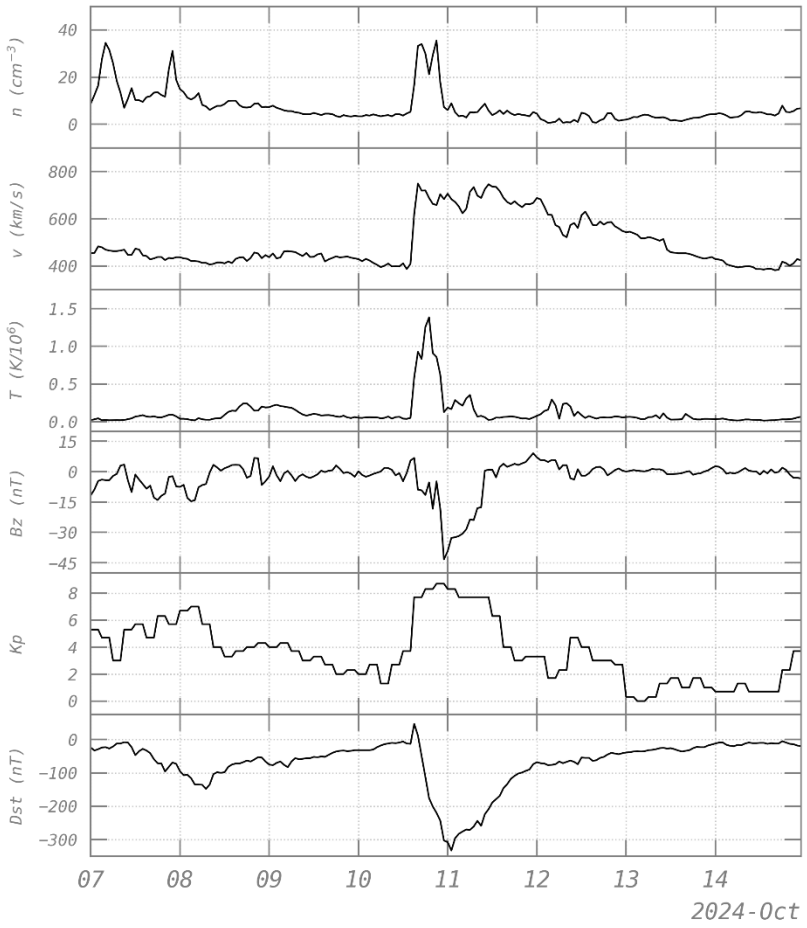

Figure 10. Solar wind density n, velocity v, temperature T, southward component of the interplanetary magnetic field Bz, geomagnetic indices Kp and Dst from 7 to 14 October 2024.

In Figure 10, the arrival of the energetic solar wind particles initiating the strong geomagnetic storm is well visible in the evening of 10 October 2024 (Dst = -335 nT, Kp=9-), preceded by a smaller event (Dst = -153 nT, Kp=7) starting on 7 October due to a peak of solar wind density. Both give effects visible in the ionosphere.

4.2. Ionospheric VTEC

Figure 11 shows that the two geomagnetic storms led, at the three different latitudes, to high variations of VTEC during the main phase of the storm (see red line). The VTEC variability reach 2 TECu/5min in the North and South. However, the storm impact is different in the southern location. Indeed, while the variability is high, the VTEC does not show rapid variations, but a smooth abnormal VTEC increase (red line, Figure 11c) compared to the expected behaviour with a maximum of differences at 21:10 UTC up to +35 TECu.

Preprints.org (www.preprints.org) | NOT PEER-REVIEWED | Posted: 24 January 2025 doi:10.20944/preprints202501.1791.v1

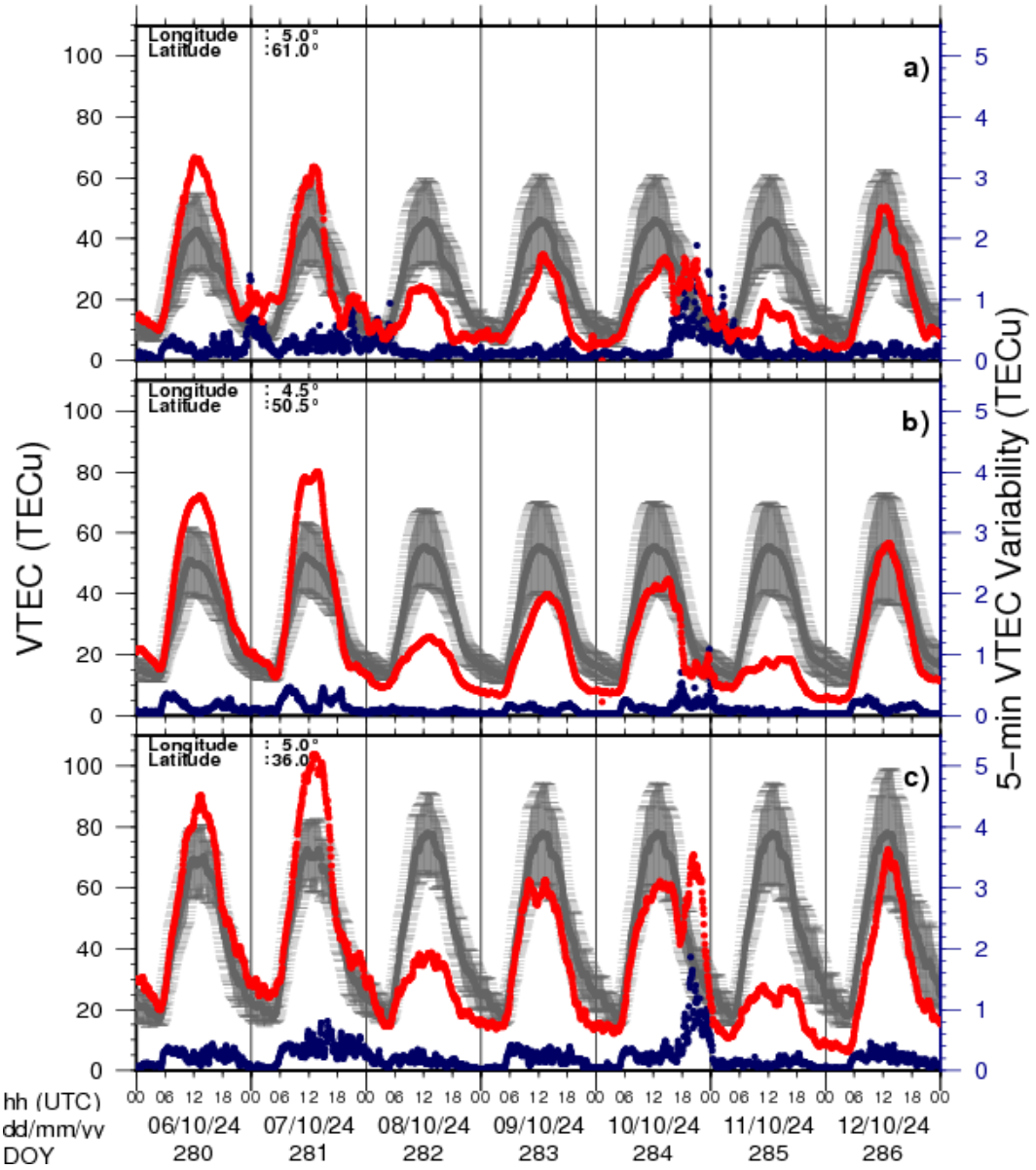

Figure 11. VTEC time series at the same 3 locations as in Figure 4 from 7 to 13 October 2024 included.

Figure 12 shows the state of the ionosphere during this maximum VTEC difference observed in the southern location at low latitude. As we can see, the VTEC observed is more than 30 TECu higher than the expected values. This is not seen ionosonde electron density observed by the ionosonde in Spain (see Figure 13, EB040) where no significant increase is observed. This difference between VTEC and electron density from ionosonde can be interpreted as an increase of the electron density above the F2 layer up to the plasmapause. This density peak is followed by a sharp decrease, leading to a value lower than the averaged density of the quiet times (gray line) during the night and the full next day and night. This after-storm depletion stands ~1.5 days (until the 12th 08:00 UTC) as seen for the mother storm day, with a minimum of -55 TECu in the low latitude the 11 May at 13:50 UTC.

 doi:10.20944/preprints202501.1791.v1

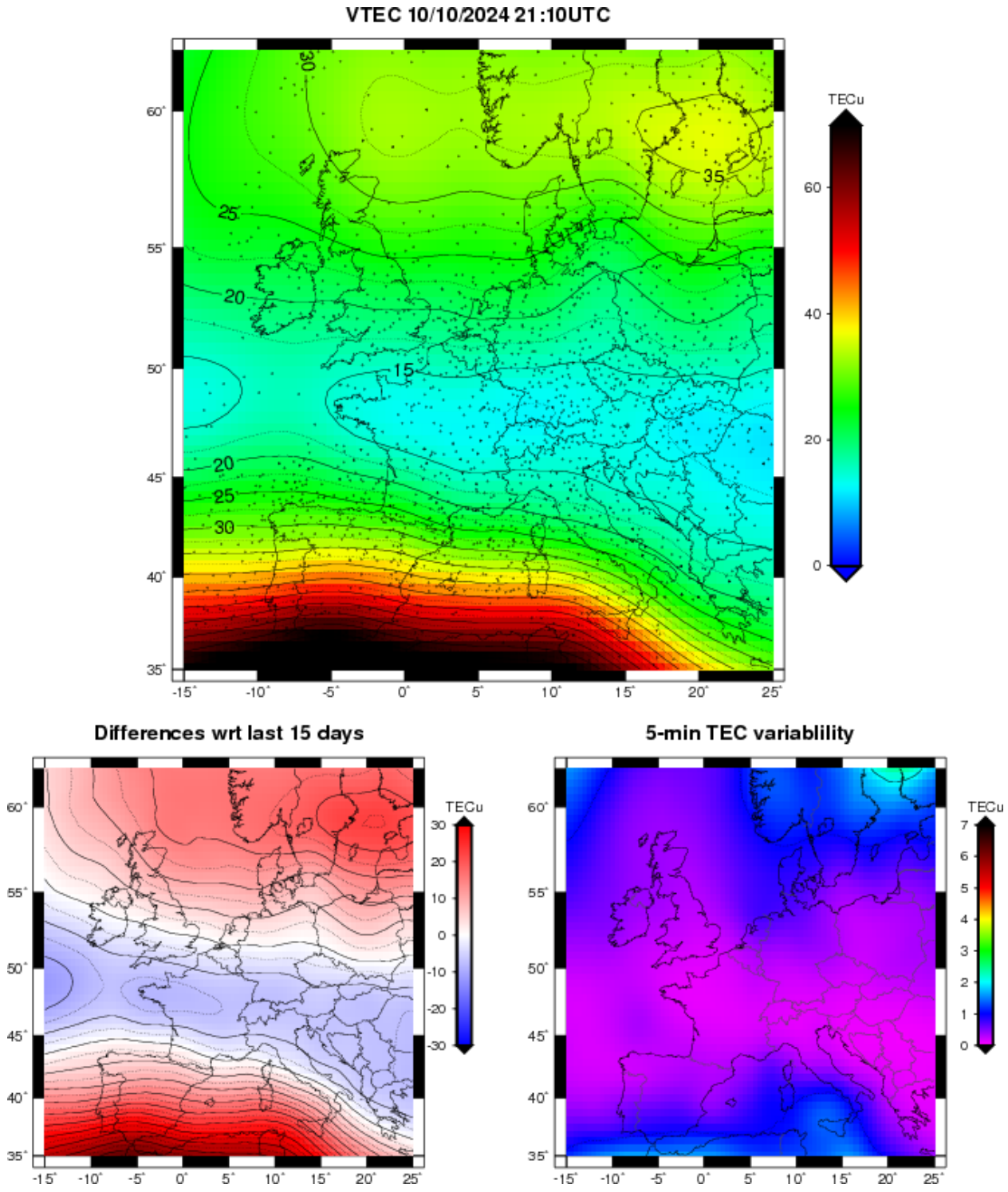

Figure 12. VTEC maps, differences with expected behaviour and variability over Europe on 10th October 2024 at 21:10 UTC. Top: VTEC maps estimated in real-time. The dots represent the VTEC data used for the interpolation. Bottom left: differences between VTEC maps and the expected VTEC (median over the past 15 days). Bottom right: the VTEC variability reflecting the ionospheric state variations during the 5-min time span of the interpolation.

4.3. Ionosonde Observations

Figure 13 shows the equivalent observations as Figure 6 but for the storm of 11 October 2024. The climatological conditions in October are different from those during the May event. The foF_1 peak is not as pronounced in October as it is in May. On the other hand, the foF_2 is slightly higher during the October event than during the May storm.

 doi:10.20944/preprints202501.1791.v1

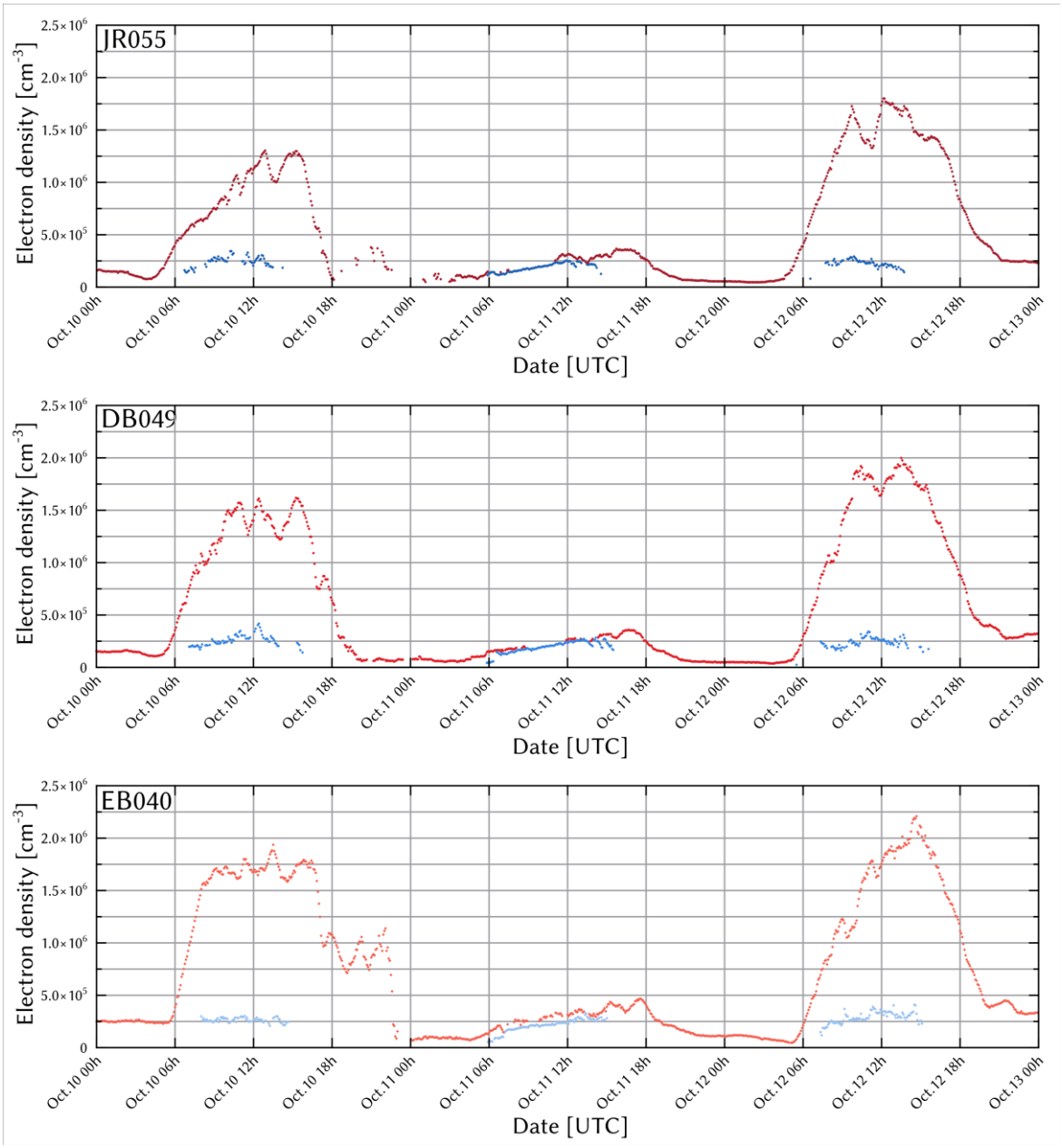

Figure 13. Peak electron densities for F_2 (red) and F_1 (blue) for the JR055 (top), DB049 (middle) and EB040 (bottom) ionosondes from 10 to 13 October 2024 0:00 UTC. Note that the maximum density (vertical axis) is here 2.5×10^6 (instead of 1.5×10^6 as in Figure 6 and 7).

Note that there are again some gaps in the time series, in particular during the night of the storm at the highest latitude observatory (JR055). These are primarily due to the presence of particle induced sporadic layers precluding observing the F region of the ionosphere. Blanketing of observations by regular Es layers is not important for this event as such layers are more rarely present at these observatories in October as compared to May.

At the onset of the storm, a steep drop in the F_2-layer density can again be observed, indicating the sudden depletion of the ionospheric plasma. The main phase and recovery, on the other hand, look different for this storm. The cases of G-condition being observed are limited, in particular in the southernmost observatory, and the background conditions were restored already in the morning of 12 October.

Figure 14 shows the critical frequencies observed by the American and Korean ionosondes. Once again, it should be noted that the F_1-peak is not as clearly observed as during the May event, and that the foF_2 values are slightly higher. At these observatories, no G-condition was observed. This is due

 doi:10.20944/preprints202501.1791.v1

to the local time of the onset of the storm. As can be seen from Figure 13, the period of G-condition observed by the European ionosondes was relatively short, compared to what was seen during the May event, from around 06:00 to around 12:00 UTC at JR055. This coincides with a period when no F_1 layer is detected at MHJ45 and IC437, so there can be no G-condition.

Some depletion of the F_2 layer during the first day after the storm can still be seen at both observatories though. In both cases, the *foF*$_2$ at the end of the period has not yet recovered entirely to the values seen before the storm. In addition, the presence of large-scale travelling ionospheric disturbances can be seen. Especially during 11 October at IC437, there are periodic oscillations evident in *foF*$_2$.

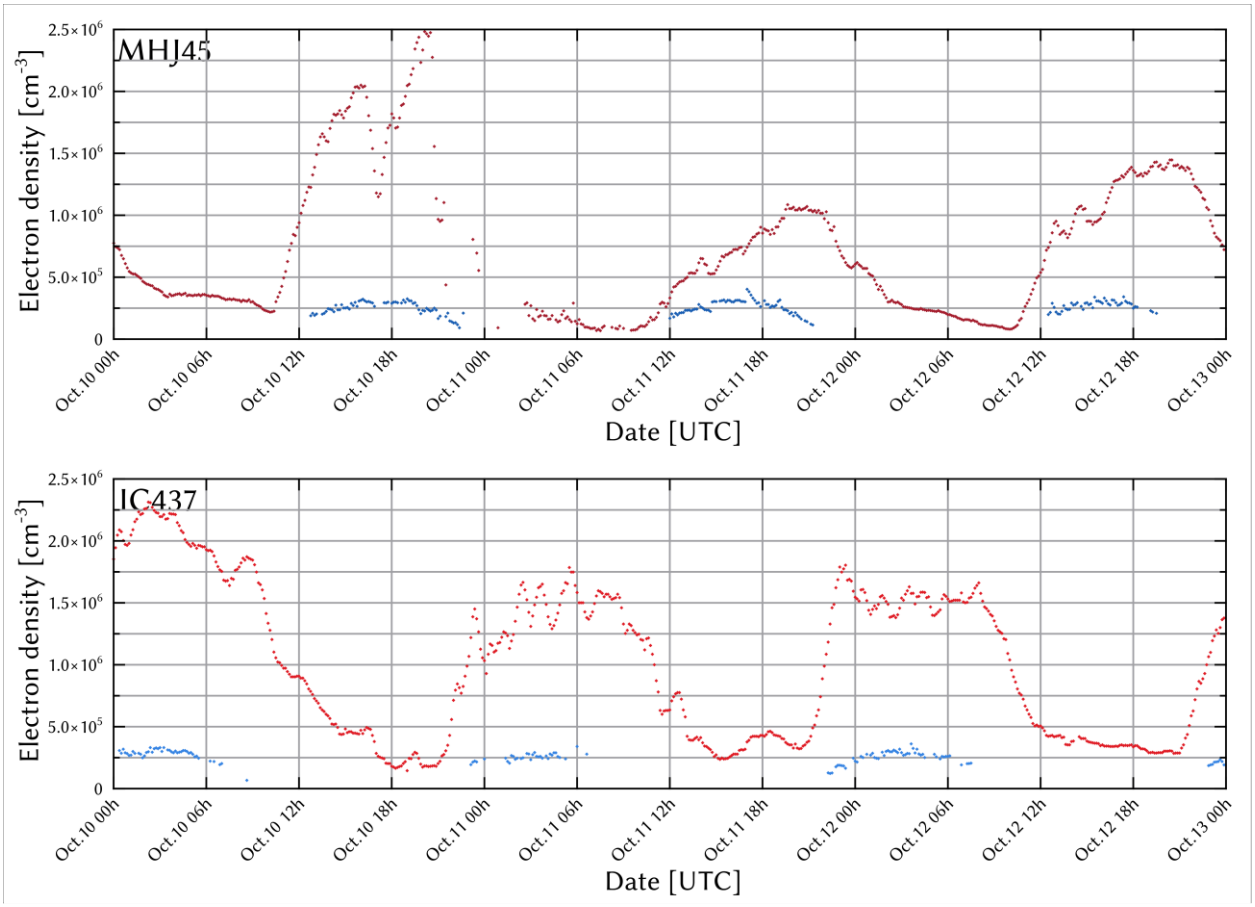

Figure 14. Time series of foF$_1$ (blue) and foF$_2$ (red) observed by the MHJ45 and IC437 ionosondes during the 11 October storm. Notice that the vertical axes are again extended to.

4.4. Plasmasphere

The BSPM model shows that on 10 October 2024 12:00 UT, before the superstorm, the plasmasphere is already anisotropic in the geomagnetic equatorial plane (see Figure 15 top left panel) due to the previous storm of 8 October. On 10 October 22:00 UT, during the storm, a double plume that extends up to 6 Re appears in the afternoon MLT sector (see Figure 15 bottom left panel). Like for all storms, the plumes rotate with the Earth (Pierrard et al., 2021b). The plasmasphere is eroded and a plasmapause close to the Earth around 2.4 Re is found at after midnight MLT ~ 3.

Preprints.org (www.preprints.org) | NOT PEER-REVIEWED | Posted: 24 January 2025 doi:10.20944/preprints202501.1791.v1

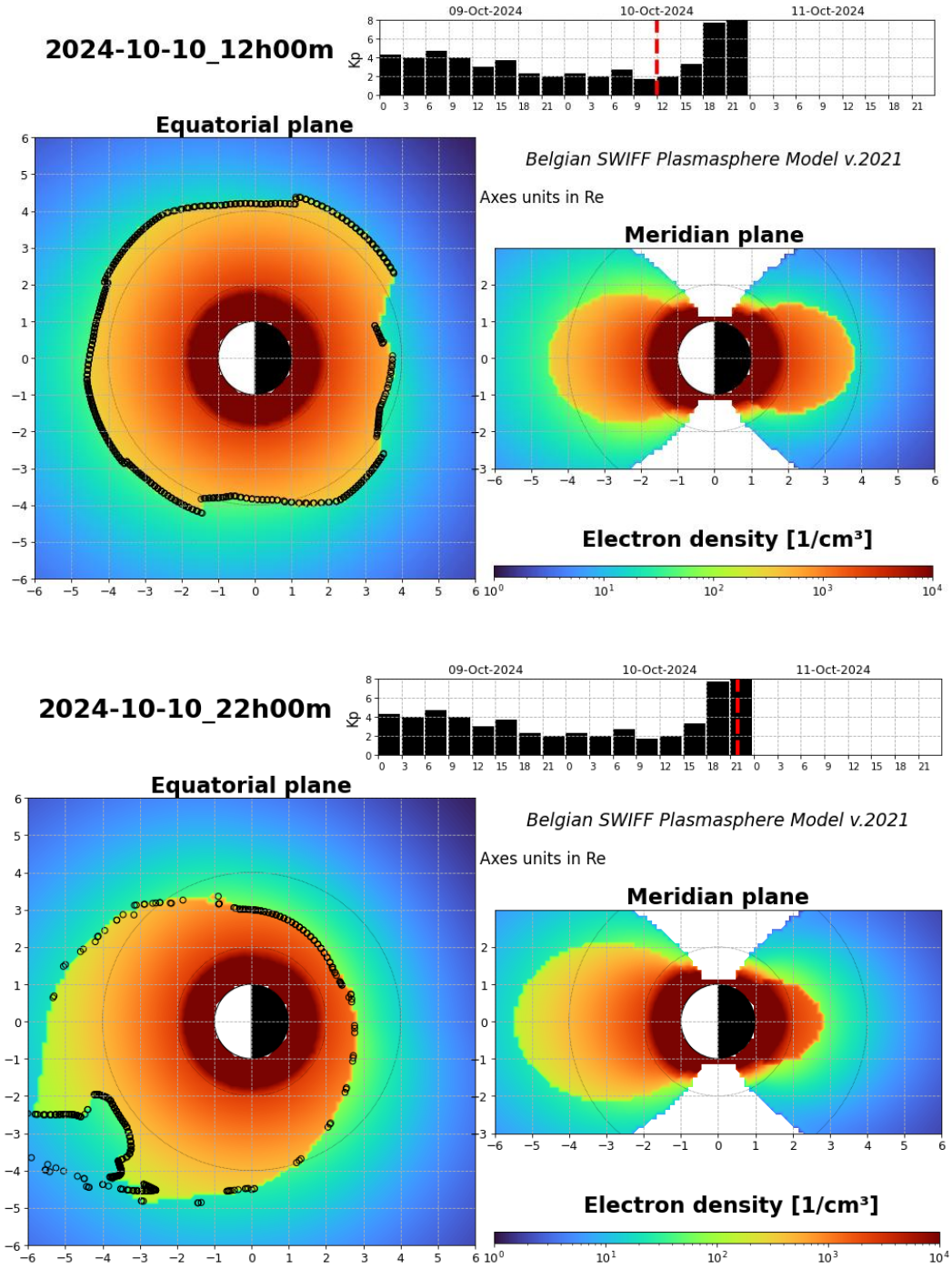

Figure 15. Electron density obtained with the BSPM plasmasphere model coupled to the ionosphere on 10 October 2024 at 12:00 UTC (before the superstorm, top panels) and 10 October 2024 at 22:00 UTC (during the superstorm, bottom panels).

A lower position of the plasmapause at 2 Re is even observed by SWARM at midnight MLT (see Figure 16), at least on 11 October, while no measurements are accessible on 10 October 2024. These exceptional observations of Kp>8+ allow us to improve the BSPM model, by increasing the extrapolated intensity of the electric field model for such high Kp values, since the empirical E5D model (McIlwain, 1986) had been validated only for lower values of Kp due to insufficient strong events.

 doi:10.20944/preprints202501.1791.v1

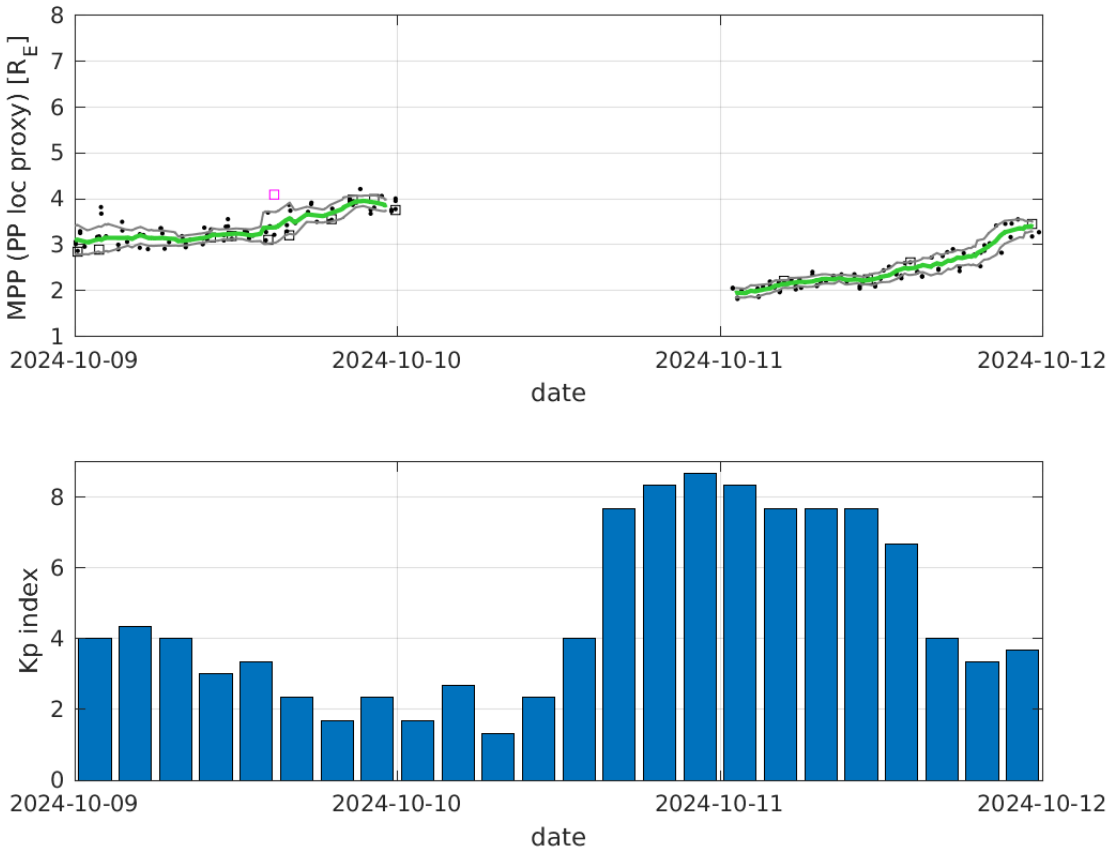

Figure 16. Midnight plasmapause proxy derived from the magnetic and plasma observation of the low-Earth orbiting Swarm satellites (like in Figure 9) from 9 to 12 October 2024.

5. Discussion and Conclusions

In the present work, we show that a study of the ionospheric observations as a function of the latitude and the Magnetic Local Time using VTEC, ionosondes and plasmaspheric observations is crucial for understanding the causes of the density variations associated with the magnetic storms. We have analysed the electron density measured by ionosondes in the F_1 and F_2 layers, the VTEC measured from the ground to GNSS satellites, and the position of the midnight plasmapause measured by SWARM during the two biggest geomagnetic storms of the present solar cycle 25, in May and October 2024. The observations at different latitudes and longitudes allow us to determine the spatial and temporal effects, and to study the fraction of electron density due to the ionospheric peak and to the plasmaspheric storm response.

The observations during the two analysed storms show that, while the ionization increases during the main phase of the storms, the density of electrons decreases for at least one day after the storms. The VTEC depletion is not only due to a decrease of the ionization in the F_2 layer, but also to a closer plasmapause. This was also observed in previous studies. For instance, Gallagher et al. (2021) found that the plasmasphere can lose 40% or more of its total mass during massive erosions. The relative contribution of the plasmasphere to the nighttime (i.e. locally) total electron content (TEC) can easily go beyond 80% during severely disturbed periods (Klimenko et al., 2015).

Nevertheless, clear differences could be observed in the response of the ionospheric layers to both storms. The storms were similar in strengths and in local time of the onset. However, the background conditions of the ionosphere in May and October are very different, at least in the lower ionosphere. The F_1 peak is more pronounced in May than in October, but the F_2 peak is more compact in October, with a peak density somewhat higher than in May. These differences in the structure of

 doi:10.20944/preprints202501.1791.v1

the ionospheric layers lead to the effects of the storm being visible for a longer time for the May event, with the F_2 layer only becoming visible again during the second day after the storm. G-condition (i.e. when F_2 layer is not detected because the density is higher in the F_1 layer than in F2) is observed for the entirety of 11 May while it is almost absent in October 2024. Such seasonal differences are smaller at higher altitudes.

The spectacular loss of F_2-layer ionization observed during both storms can be due to an increase of the recombination rates, associated to a higher temperature and density caused by the injection of particles, in combination with outflow of ionization.

Data Availability Statement : Omni data were retrieved from https://omniweb.gsfc.nasa.gov/html/ow_data.html, Dst data from https://wdc.kugi.kyoto-u.ac.jp/. The BSPM model is accessible on https://esc.pithia.eu/. VTEC is available on STCE.be. SWARM plasmapause proxy is found at https://swe.ssa.esa.int/elte-plasma-federated. A detailed description of all these new SWARM products as well as the detailed description of the processing algorithm can be found at https://earth.esa.int/eogateway/activities/plasmapause-related-boundaries-in-the-topside-ionosphere-as-derived-from-swarm-measurements (PRISM docs). The algorithm for SWARM detection, and the derivation of plasmapause index is published also in Heilig and Lühr (2018). This publication uses data from the ionospheric observatory in Roquetes, Spain, owned and operated by the Fundació Observatori de l'Ebre, and from the Juliusruh Ionosonde, which is owned by the Leibniz Institute of Atmospheric Physics Kuehlungsborn. All ionograms used are available from the GIRO repository (giro.uml.edu).

Acknowledgments: The project 21GRD02 BIOSPHERE has received funding from the European Partnership on Metrology, co-financed from the European Union's Horizon Europe Research and Innovation Programme and by the Participating States. The authors thank the Horizon 2020 research and innovation programme funding from the European Union for the PITHIA-NRF project (Plasmasphere Ionosphere Thermosphere Integrated Research Environment and Access services) with Grant Agreement 101007599.

Author Contributions: Conceptualization, V.P.; methodology, V.P., T.V.; software, all; validation, V.P., T.V.; formal analysis, all authors; investigation, all; resources, V.P.; data curation, T.V., J.M.C., N.B.; writing---original draft preparation, V.P.; writing---review and editing, all; visualization, all; supervision, V.P.; project administration, V.P.; funding acquisition, V.P. All authors have read and agreed to the present version of the manuscript.

Conflicts of Interest: The authors declare no conflict of interest.

References

1. Bandic M., G. Verbanac, V. Pierrard, and J. Cho (2017), Evidence of MLT propagation of the plasmapause inferred from THEMIS data, J. Atmosph. Sol.-Terr. Phys., 161, 55-63, doi: 10.1016/j.jastp.2017.05.005, 2017
2. Bergeot N., Tsagouri I., Bruyninx C., Legrand J., Chevalier J.-M., Defraigne P., Baire Q. and Pottiaux E., The influence of space weather on ionospheric total electron content during the 23rd solar cycle, J. Space Weather Space Clim., 3 (2013) A25, doi: 10.1051/swsc/2013047
3. Bergeot N., Chevalier J.-M., Bruyninx C., Pottiaux E., Aerts W., Baire Q., Legrand J., P. Defraigne and W. Huang, Near real-time ionospheric monitoring over Europe at the Royal Observatory of Belgium using GNSS data, J. Space Weather Space Clim., 4 A31, doi: 10.1051/swsc/2014028, 2014.
4. Bruyninx, C., Legrand, J., Fabian, A., Pottiaux E., GNSS metadata and data validation in the EUREF Permanent Network, GPS Solut 23: 106, doi: 10.1007/s10291-019-0880-9, 2019.
5. Darrouzet F., J. De Keyser and V. Pierrard (Eds), The Earth's plasmasphere: Cluster and IMAGE–A modern perspective, Springer, New York, 296p. 2009.
6. Gallagher D. L., Comfort R. H., Katus R. M., Sandel B. R., Fung S. F., and Adrian M. L., The breathing plasmasphere: Erosion and refilling. Journal of Geophysical Research: Space Physics, 126, e2020JA028727, doi: 10.1029/2020JA028727, 2021.
7. Heilig B., and Lühr H., Quantifying the relationship between the plasmapause and the inner boundary of small-scale field-aligned currents, as deduced from Swarm observations, Annales Geophysicae, 36, 595–607, doi: 10.5194/angeo-36-595-2018, 2018.
8. Heilig B., Stolle C., Kervalishvili G., Rauberg J., Miyoshi Y., Tsuchiya F., et al., Relation of the plasmapause to the midlatitude ionospheric trough, the sub-auroral temperature enhancement and the distribution of small-scale field aligned currents as observed in the magnetosphere by THEMIS, RBSP, and Arase, and in

the topside ionosphere by Swarm, Journal of Geophysical Research: Space Physics, 127, e2021JA029646, doi: 10.1029/2021JA029646, 2022.

9. Karan D.K., Martinis C.R., Daniell R., Eastes R.W.,Wang W., McClintock W.E., Michell R.G., England S.L., GOLD observations of the merging of the Southern Crest of the equatorial ionization anomaly and aurora during the 10 and 11 May 2024 Mother's Day super geomagnetic storm, Geophys. Res. Lett., 51, e2024GL110632, 2024.
10. Kauristie, K., J. Andries, P. Beck, J. Berdermann, D. Berghmans, C. Cesaroni et al., Space Weather Services for Civil Aviation—Challenges and Solutions, Remote Sensing, 13(18), 3685, doi:10.3390/rs13183685, 2021.
11. Klimenko M.V., Klimenko V.V., Zakharenkova I.E., Cherniak I.V., The global morphology of the plasmaspheric electron content during northern winter 2009 based on GPS/COSMIC observation and GSM TIP model results, Adv. Space Res., 55, 2077–2085, 2015.
12. Knudsen D. J., Burchill J. K., Buchert S. C., Eriksson A. I., Gill R., Wahlund J.-E., et al., Thermal ion imagers and Langmuir probes in the Swarm electric field instruments. *Journal of* Geophysical Research: Space Physics, 122, 2655–2673, doi: 10.1002/2016JA022571, 2017.
13. Mcllwain C.E., A *Kp* Dependent Equatorial Electric Field Model: The Physics of Thermal Plasma in the Magnetosphere, Adv. Space Res., 6(3), 187–197, 1986.
14. Mendillo, M., Storms in the ionosphere: patterns and processes for total electron content, Rev. Geophys., 44, RG4001, doi: 10.1029/2005RG000193, 2006.
15. Mošna Z., V. Barta, K.A. Berényi, J. Mielich, T. Verhulst, D. Kouba, et al., The March and April 2023 ionospheric storms over Europe, Frontiers in Astronomy and Space Science, 11, 1462160, doi: 10.3389/fspas.2024.1462160, 2024.
16. Olsen N., Friis-Christensen E., and Floberghagen R., The Swarm Satellite Constellation Application and Research Facility (SCARF) and Swarm data products, Earth Planet Sp,, 65(1), doi: 10.5047/eps.2013.07.001, 2013.
17. Pierrard V., Effects of the Sun on the space environment of the Earth, Presses Universitaires de Louvain, ISBN: 978-2-39061-442-5, 208 p., https://i6doc.com/en/book/?gcoi=28001100628290, 2024.
18. Pierrard V., E. Botek, and F. Darrouzet, Improving Predictions of the 3D Dynamic Model of the Plasmasphere, 8, 69, Front. In Astron. Space Sci., 8:681401, doi: 10.3389/fspas.2021.681401, 2021a.
19. Pierrard V., E. Botek, J.-F. Ripoll, S. A. Thaller, M. B. Moldwin, M. Ruohoniemi, and G. Reeves, Links of the plasmapause with other boundary layers of the magnetosphere: ionospheric convection, radiation belts boundaries, auroral oval, Frontiers in Astronomy and Space Sciences, 8, doi: 10.3389/fspas.2021.728531, 2021b.
20. Pierrard V., and J. Cabrera, Comparisons between EUV/IMAGE observations and numerical simulations of the plasmapause formation, Annales Geophysicae, 23, 7, 2635-2646, doi: 10.5194/angeo-23-2635-2005, SRef-ID: 1432-0576/ag/2005-23-2635, 2005.
21. Pierrard V. and J. Cabrera, Dynamical simulations of plasmapause deformations, *Space Science Reviews*, 122, 1-4, 119-126, doi: 10.1007/s11214-005-5670-8, 2006.
22. Pierrard V., and K. Stegen, A three dimensional dynamic kinetic model of the plasmasphere, Journal Geophys. Res., 113, A10209, doi: 10.1029/2008ja013060, 2008.
23. Pierrard V., and M. Voiculescu, The 3D model of the plasmasphere coupled to the ionosphere, Geophys. Res. Lett., 38, L12104, doi: 10.1029/2011GL047767, 2011.
24. Pierrard V., A. Winant, E. Botek, and M. Péters de Bonhome, The Mother's Day solar storm of 11 May 2024 and its effect on Earth's radiation belts, Universe, 10, 10, 391, doi: 10.20944/preprints202409.1134.v1, 2024.
25. *Reinisch, B. W., and I. A. Galkin, Global ionospheric radio observatory (GIRO), Earth, Planets, and Space, 63, 377-381, doi:10.5047/eps.2011.03.001, 2011.*
26. Ripoll J.-F., V. Pierrard, G. S. Cunningham, X. Chu, K. A. Sorathia, D. P. Hartley, S. A. Thaller, V. G. Merkin, G. L. Delzanno, S. De Pascuale, A. Y. Ukhorskiy, Modeling of the cold electron plasma density for radiation belt physics, Front. Astron. Space Sci., 10:1096595, doi: 10.3389/fspas.2023.1096595, 24 Feb 2023.
27. Ripoll, J.-F., S. Thaller, D. Hartley, D. Malaspina, W. Kurth, G. S. Cunningham, V. Pierrard, J. Wygant, Statistics and models of the electron plasma density from the Van Allen Probes, Journal of Geophys. Res.:

 doi:10.20944/preprints202501.1791.v1

Space Physics, Journal of Geophys. Res.: Space Physics, 129, e2024JA032528, doi: 10.1029/2024JA032528, 16 July 2024.

28. Spogli L., et al., The effects of the May 2024 Mother's Day superstorm over the Mediterranean sector: from data to public communication, Annals of Geophysics, 67, 2, 218, doi: 10.4401/ag-9117, 2024.
29. Tsagouri I., Belehaki A., Koutroumbas K., Tziotziou K., and Herekakis T., Identification of Large-Scale Travelling Ionospheric Disturbances (LSTIDs) Based on Digisonde Observations, Atmosphere, 14(2):331, doi: 10.3390/atmos14020331, 2023.
30. Verbanac G., V. Pierrard, M. Bandic, F. Darrouzet, J.-L. Rauch, and P. Décréau, Relationship between plasmapause, solar wind and geomagnetic activity between 2007 and 2011 using Cluster data, Annales Geophysicae, Ann. Geophys., 33, 1271-1283, doi:10.5194/angeo-33-1271-2015, 2015.